RSC Advances

PAPER

View Article Online
View Journal | View Issue

Cite this: *RSC Adv.*, 2025, **15**, 35573

Zincronized NiCo selenides coupled with polypyrrole: a synergistic route to high-energy asymmetric supercapacitors

Anique Ahmed,†[a] Muhammad Ramzan Abdul Karim †*[b] and Muhammad Usman[a]

Transition metal selenides have gained significant attention for energy storage applications due to their outstanding electrochemical properties, excellent theoretical capacity, superior conductivity, and eco-friendly nature. The dual strategy consists of incorporating zinc into nickel cobalt selenide to optimize its electronic structure and redox kinetics, combined with the integration of a conductive polymer matrix to enhance the charge transport mechanism. However, there is still room for improvement in energy density and storage capability which can be achieved *via* composites with conducting polymers. To enhance the electrochemical performance of $NiCoSe_2$–Zn15, polypyrrole (PPy) was incorporated through a physical mixing approach. This strategic modification significantly improved electrical conductivity, ion diffusion, and structural stability of the synthesized electrode material. Different structural and morphological characterization methods have been employed to verify the successful synthesis of the selenide materials. The electrochemical performance of all electrodes in the three-electrode configuration was evaluated, revealing that the $NiCoSe_2$–Zn15/30PPY sample exhibited remarkable results. The optimized sample demonstrated outstanding specific capacities of 2252.6 C g^{-1} at 2 mV s^{-1} and 1370.5 C g^{-1} (1957.9 F g^{-1}) at 0.5 A g^{-1}. Most importantly, the $NiCoSe_2$–Zn15/30PPY||AC supercapattery device was successfully fabricated, achieving an energy density of 130.7 Wh kg^{-1} and a power density of 11 900 W kg^{-1}. The hybrid device exhibited excellent cyclic stability, retaining 94.3% of its initial capacity after 5000 cycles. The hybrid nature of the $NiCoSe_2$–Zn15/30PPY||AC was further validated using Power's law and Dunn's model. This study highlights the potential of selenide-based nanocomposites as viable battery-grade electrode materials in asymmetric supercapacitor (ASC) devices.

Received 18th June 2025
Accepted 11th September 2025

DOI: 10.1039/d5ra04328j

rsc.li/rsc-advances

1. Introduction

The growing demand for portable technology and electric vehicles has driven significant research efforts toward the development of energy storage systems that offer affordability, safety, and efficiency.[1–3] Among electrochemical energy storage technologies, supercapacitors (SCs) stand out as a preferred choice owing to their rapid charge/discharge features, high power density, extended cycle life, and superior safety features.[4,5] Although supercapacitors demonstrate outstanding power capabilities, their relatively low energy density (E_s) presents a significant challenge for widespread commercialization.[6,7] Hybrid supercapacitors (HSCs), which incorporate both battery-type (pseudocapacitive) electrode materials and electric double-layer capacitors (EDLCs), demonstrate significant potential for achieving high energy and power density, rapid charging/discharging features, and long-term stability.[8–11] The pseudocapacitive electrode materials, including transition metal oxides, chalcogenides, and conducting polymers, provide a higher energy density than EDLCs.[12,13] Nevertheless, their low-rate capability presents a challenge for their application in high-power systems.[14] Conversely, carbonaceous materials including activated carbon, CNTs, and graphene, are primarily used as electrode materials in EDLCs due to their ability to store electrical energy *via* surface charge accumulation.[15] While EDLC electrodes demonstrate remarkable cycling stability and high-power density (P_s), they are limited by low energy density.[16] To fabricate high-performance HSCs that address the limitation of energy density, it is imperative to investigate appropriate battery-type electrode materials and strategically modify their electrochemical characteristics.[9] Recently, extensive research has been conducted on transition metal dichalcogenides (TMDs) due to their cost-effectiveness and environmental compatibility.[17,18] TMDs are expressed by the chemical formula MX_2, where M stands for a transition metal taken group IV to VII, and X represents a chalcogen, which may be tellurium (Te), selenium (Se), or sulfur (S).[19,20] TMDs, particularly Zn, Ni, and

[a]*Faculty of Engineering Sciences, Ghulam Ishaq Khan Institute of Engineering Sciences and Technology, Topi, 23640, Khyber Pakhtunkhwa, Pakistan*

[b]*Faculty of Materials and Chemical Engineering, Ghulam Ishaq Khan Institute of Engineering Sciences and Technology, Topi, 23640, Khyber Pakhtunkhwa, Pakistan. E-mail: ramzan1109@hotmail.com; ramzan.karim@giki.edu.pk*

† Authors contributed equally and share first authorship.

Co-based selenides, are being extensively studied due to their remarkable theoretical capacity, which makes them potential electrode materials for next-generation batteries.[21,22] The presence of multiple valence states enables them to facilitate reversible redox reactions efficiently.[23] Despite their high theoretical capacity, experimental studies have demonstrated that the actual capacities of these selenides materials is significantly lower.[24] The low-rate capacity of selenium-based TMDs is often attributed to their poor conductivity, slow reaction kinetics, and limited redox active sites.[25] These challenges represent significant barriers to their widespread application in electrochemical energy storage systems. To address these challenges, researchers are investigating various strategies and alternative electrode materials for integration with TMDs.[26,27]

Among various TMDs, transition metal selenides, particularly nickel (Ni)-cobalt (Co) selenides have attracted considerable interest because of their outstanding electrochemical activity, favorable conductivity, and multiple oxidation states, making them promising electrode materials.[21,28] Extensive research has highlighted that the synergistic interaction between the two metal (Ni and Co) cations in NiCo bimetallic selenides results in superior electrochemical performance compared to monometallic selenides, which significantly improves conductivity and enables efficient multi-electron redox reactions.[28–30] Despite their promising electrochemical properties, NiCo selenides suffer from inadequate structural stability and slow reaction kinetics.[31] These limitations significantly affect its long-term cycling performance and rate capability, which ultimately hinder their potential for large-scale applications.[32] To overcome these issues, incorporating other materials into the nickel-cobalt selenides has emerged as a promising strategy to improve charge storage capabilities by leveraging the synergistic effects of multiple active components.[33] The incorporation of zinc (Zn) into the nickel cobalt selenide ($NiCoSe_2$) matrix effectively addresses these issues by enhancing the structural stability and rate capability of the material. The presence of Zn introduces additional active sites, improving the electrochemical redox reactions while also reinforcing the material's overall mechanical stability, leading to better cycling performance.[34,35] Despite these improvements, Zn incorporation alone was not fully optimizing the electrode's performance, as it negatively affects two other critical parameters such as ion diffusion efficiency and electrode volume expansion during charge/discharge cycles.[36] Various approaches have been explored to overcome the aforementioned challenges. In this context, the incorporation of conducting polymers (including polythiophene, PPy, and polyaniline) or carbonaceous materials (such as carbon nanofibers, reduced graphene oxide, amorphous carbon, 3D graphene, and carbon nanotubes) as dopants plays a crucial role in preventing the aggregation of active species.[37,38] Additionally, these dopants significantly enhance the electrical conductivity, rate capability, and cyclic stability of transition metal selenides based electrode materials.[21,39,40] This finding encourages us to integrate PPy with mixed metal selenides, aiming to improve ion diffusion efficiency and electrical conductivity. The molecular-level interaction between these materials exhibits a remarkable synergistic effect, resulting in a novel battery-type hybrid electrode material with significantly enhanced specific capacity (Q_s) and long-term stability compared to pristine materials.

Herein, Zn-doped nickel cobalt selenide (mixed metal) was successfully synthesized *via* a hydrothermal approach. The doped mixed metal selenide is subsequently combined with PPy through a physical mixing process to form a composite. Elemental composition, surface morphology, and crystalline structure of the synthesized nanomaterials were characterized using energy-dispersive X-ray (EDX) spectroscopy, scanning electron microscopy (SEM), and X-ray diffraction (XRD), respectively. The electrochemical performance of the synthesized materials was evaluated using a three-electrode cell configuration with 1 M KOH as the electrolyte solution. The electrode demonstrating the most enhanced electrochemical response was subsequently incorporated into the design of a hybrid (asymmetric) supercapacitor. A two-electrode cell was employed to examine the real-performance of the fabricated device, while computational simulations were used to analyze its energy storage behavior in terms of capacitive and diffusive contribution.

2. Experimental

2.1. Materials and chemicals

Zinc(II) nitrate hexahydrate ($Zn(NO_3)_2 \cdot 6H_2O$), polyvinylidene fluoride (PVDF), hydrazine hydrate ($N_2H_4 \cdot XH_2O$, 50–60%), cobalt (II) nitrate hexahydrate ($Co(NO_3)_2 \cdot 6H_2O$), polypyrrole (PPy), sodium selenite ($Na_2SeO_3 \cdot 5H_2O$), activated carbon (AC), nickel(II) nitrate hexahydrate ($Ni(NO_3)_2 \cdot 6H_2O$), *N*-methyl-2-pyrrolidone (NMP), potassium hydroxide (KOH), ammonium persulfate ($(NH_4)_2S_2O_8$), and acetylene black (AB), ethanol, and acetone were obtained from Sigma-Aldrich.

2.2. Synthesis of $NiCoSe_2$–Zn15

The hydrothermal synthesis of $NiCoSe_2$ with 15% Zn incorporation was carried out through a multi-step process. The solution 1 was obtained by dissolving 0.786 g of $Ni(NO_3)_2 \cdot 6H_2O$, 0.735 g of $Co(NO_3)_2 \cdot 6H_2O$, and 0.134 g of $Zn(NO_3)_2 \cdot 6H_2O$ in 35 mL of deionized (DI) water while continuously stirring for 30 minutes. Meanwhile, a sodium selenite (Na_2SeO_3) solution was obtained by adding 0.343 g of Na_2SeO_3 in 15 mL of DI water, followed by 15 minutes of stirring. Subsequently, solution 1 was introduced dropwise into the sodium selenite solution and stirred continuously during the process. To enhance the reduction process, 3 mL of hydrazine hydrate (N_2H_4) was introduced into the mixture, followed by an additional 1 hour of continuous stirring. The resulting homogeneous mixture was then shifted to the autoclave with Teflon-lined stainless-steel (100 mL) and exposed to hydrothermal conditions at 160 °C for 24 hours. After the reaction was complete, the autoclave was left at room temperature to cool down gradually and the resulting product was separated and cleaned multiple times with DI water and absolute ethanol to get rid of any unreacted residues. Finally, the pure product was kept in a vacuum-oven at

Fig. 1 Schematic overview of the, (a) hydrothermally synthesized $NiCoSe_2$–Zn15. (b) Physical mixing of $NiCoSe_2$–Zn15 with PPy.

75 °C for a total of 10 hours, resulting in the $NiCoSe_2$–Zn15. Fig. 1(a) illustrates the hydrothermal synthesis of the mixed metal selenides.

2.3. Synthesis of PPy

Chemical oxidative polymerization was employed for the synthesis of PPy. Initially, $(NH_4)_2S_2O_8$ was added in 100 mL of DI water while stirring constantly for 15 min at a controlled temperature of 0 °C to create a uniform reaction medium. Subsequently, 0.15 mol of pyrrole monomer was dissolved dropwise into the oxidant solution while maintaining constant stirring to facilitate controlled polymerization. The reaction was allowed to proceed at 0 °C for 16 hours, during which the gradual formation of a black precipitate indicated successful PPy polymerization. The obtained polymer was separated through filtration and thoroughly washed with deionized (DI) water, ethanol, and methanol (three cycles each) to separate any unreacted precursors or byproducts. The final step was to dry the purified PPy powder in a vacuum oven at 70 °C for 14 hours, the final product was named as PPy.

2.4. Synthesis of $NiCoSe_2$–Zn15/PPy composites

PPy was incorporated into the $NiCoSe_2$–Zn15 composite through a physical mixing process. Initially, $NiCoSe_2$–Zn15 was dispersed in 30 mL of DI water under continuous stirring for 3 hours at room temperature. Subsequently, 10% PPy was introduced into the mixture, and stirring was continued to ensure uniform distribution. The resultant suspension was shifted for centrifugation and then dried in a vacuum oven at 70 °C, yielding the final product is $NiCoSe_2$–Zn15/10PPy. Following the same procedure, $NiCoSe_2$–Zn15 was combined with 20% PPy to synthesize $NiCoSe_2$–Zn15/20PPy. Similarly, $NiCoSe_2$–Zn15/30PPy was prepared with the addition of 30% PPy in $NiCoSe_2$–Zn15. Finally, 40% PPy was introduced into the $NiCoSe_2$–Zn15 dispersion using the similar method to obtain $NiCoSe_2$–Zn15 with 40% PPy composition, referred to as $NiCoSe_2$–Zn15/40PPy. Physical blending was employed to obtain a uniform $NiCoSe_2$–Zn15/PPy composite. Both powders were dispersed in DI water, mixed, centrifuged, and dried, ensuring homogeneous distribution without inducing any chemical reaction.[41] This approach preserved the individual identities of the components while enhancing physical uniformity, electrical connectivity, and overall performance of the composite.[42] The physical mixing process for $NiCoSe_2$–Zn15/PPy composites are shown in Fig. 1(b).

3. Materials characterization

The electrochemical characterization of the fabricated selenide electrodes was evaluated with a GAMRY (3000 Reference) potentiostat/galvanostat system. A three-electrode setup was employed, with a platinum wire playing the role of the counter electrode and a Hg/HgO electrode being the reference electrode. An aqueous solution of 1 M KOH was utilized as an electrolyte for all experiments. In two electrode cell configurations, the selenide-based electrode ($NiCoSe_2$–15Zn/30PPy) was connected to the positive terminal, while activated carbon (AC) served as

the negative electrode to form an asymmetric (Hybrid) supercapacitor. A filter paper was placed between the two electrodes as a separator to prevent short-circuiting while allowing ionic transport. The electrochemical characterization was performed using CV, GCD, and EIS measurements. For a hybrid device to operate efficiently, accurate mass and charge balance is essential. In accordance with eqn (1), the mass and charge balance between the anode and cathode was maintained at a 4 mg active material of $NiCoSe_2$–Zn15/30PPy and 7 mg active material of AC.[43]

$$\frac{m^+}{m^-} = \frac{\Delta V^- C^-}{\Delta V^+ C^+} \quad (1)$$

Here, $\frac{m^+}{m^-}$ denote the masses of the anode and cathode, respectively, while $\frac{C^-}{C^+}$ correspond to their specific capacitances. ΔV refers to the potential window applicable to each electrode. The structural properties, elemental composition, and morphology of the synthesized materials were examined through XRD, EDX, and SEM techniques, respectively. An AXRD-LPD system was employed for XRD characterization, while SEM imaging and EDX analysis were carried out using a ZEISS EVO 15 setup.

4. Results and discussion

4.1. Structural characterization

X-ray diffraction (XRD) analysis was employed to analyze the phase structure and composition of the mixed metal selenide based synthesized materials. The XRD patterns of all samples are presented in Fig. 2(a). The XRD diffraction peaks observed for $NiCoSe_2$–Zn15 align closely with JCPDS card no: 70-2851 ($NiCoSe_2$) and JCPDS card no: 80-0008 (Zn selenide), confirming the formation of Zn doped nickel cobalt selenide ($NiCoSe_2$–Zn15).[44] The XRD pattern of pristine PPy displays a broad diffraction hump centered around $2\theta \approx 25°$, which is characteristic of its predominantly amorphous or semi-crystalline structure. This diffuse peak originates from the random orientation of polymer chains and the partial ordering of pyrrole rings, rather than from long-range crystalline domains. The absence of sharp diffraction peaks confirms the lack of significant crystallinity in PPy, which is consistent with previously reported results for conducting polymers.[45] Such amorphous features facilitate ion transport within the polymer matrix and play a crucial role in enhancing the electrochemical performance when PPy is combined with crystalline transition metal selenides.[46] In the case of $NiCoSe_2$–Zn15/10PPy, $NiCoSe_2$–Zn15/20PPy, $NiCoSe_2$–Zn15/30PPy, and $NiCoSe_2$–Zn15/40PPy the XRD spectrum show maximum diffraction peak matching with both $NiCoSe_2$–Zn15 and PPy spectra, indicating the preparation of Zn doped NiCo selenide and confirming the successful composites formation of $NiCoSe_2$–Zn15/PPy phases. The presence of well-defined and sharp diffraction peaks in the pattern confirms the crystalline nature of the synthesized material. Such crystallinity is advantageous for energy storage systems as it promotes efficient electron mobility and ion diffusion by minimizing structural defects and enhancing charge transport pathways.

The surface morphology of the mixed metal based synthesized materials was systematically examined using SEM, as shown in Fig. 2(b–g). The pristine $NiCoSe_2$–Zn15 selenide (Fig. 2(b)) exhibited a relatively rough and irregular surface with a flake-like architecture, suggesting limited surface area and suboptimal pathways for charge transport. In contrast, the PPy dopant material (Fig. 2(g)) displayed a highly porous, interconnected globular structure, which is most favorable for ion diffusion and enhances redox activity. Upon incorporating 10% PPy into the selenide matrix (Fig. 2(c)), a partial coverage of the active material was observed, with noticeable improvements in surface uniformity and porosity compared to the pristine sample, although the PPy distribution appeared somewhat discontinuous. Increasing the PPy content to 20% (Fig. 2(d)) resulted in a more uniform and interconnected composite morphology with reduced agglomeration, indicating enhanced electronic conductivity and more accessible electroactive sites. At 30% PPy incorporation (Fig. 2(e)), the material demonstrated an optimal porous network with a well-dispersed PPy coating, promoting efficient electron transport and facilitating ion diffusion, which is expected to significantly boost the electrochemical performance. However, further increasing the PPy content to 40% (Fig. 2(f)) led to excessive polymer deposition, causing particle agglomeration and partial blockage of the porous structure, potentially hindering electrolyte accessibility and reducing overall electrochemical efficiency. Among all samples, the composite with 30% PPy demonstrated the most favorable morphology, offering an optimal balance between conductivity, ion diffusion pathways, and electroactive surface area, making it the most promising candidate for high-performance hybrid (asymmetric) supercapacitor.

The elemental composition of all samples (mixed metal selenide) was evaluated through energy dispersive X-ray (EDX) spectroscopy. The corresponding EDX spectra for all samples are depicted in Fig. 3. In the spectra of $NiCoSe_2$–Zn15/10PPy, $NiCoSe_2$–Zn15/20PPy, $NiCoSe_2$–Zn15/30PPy, and $NiCoSe_2$–Zn15/40PPy characteristic Kα peaks observed around 6.9, 7.63, 8.68, and 11.2 keV are attributed to Co, Ni, Zn, and Se, respectively (Fig. 3(a)). The peak at 0.2, 0.3, and 0.5 correspond with C, N, and O, which confirm the presence of the PPy in the composite samples. Additionally, Lα peaks located at 0.84, 0.86, 0.88, and 1.12 keV further confirm the presence of Co, Ni, Zn and Se, supporting the formation of Zn doped NiCo metal selenides with PPy composites (Fig. 3(b–e)). The EDX spectrum of S1 reveals peaks corresponding to Co, Ni, Zn, and Se (Fig. 3(a)), while that of S6 exhibits the formation of PPy through peaks related to C, N, and O (Fig. 3(f)). The absence of any impurity peaks across all spectra confirms the phase purity of the synthesized products.

4.2. Electrochemical analysis

4.2.1. Cyclic voltammetry (CV). CV measurements were performed for selenide samples within a potential window (PW) of 0 to 0.7 V to investigate charge reaction kinetics, utilizing

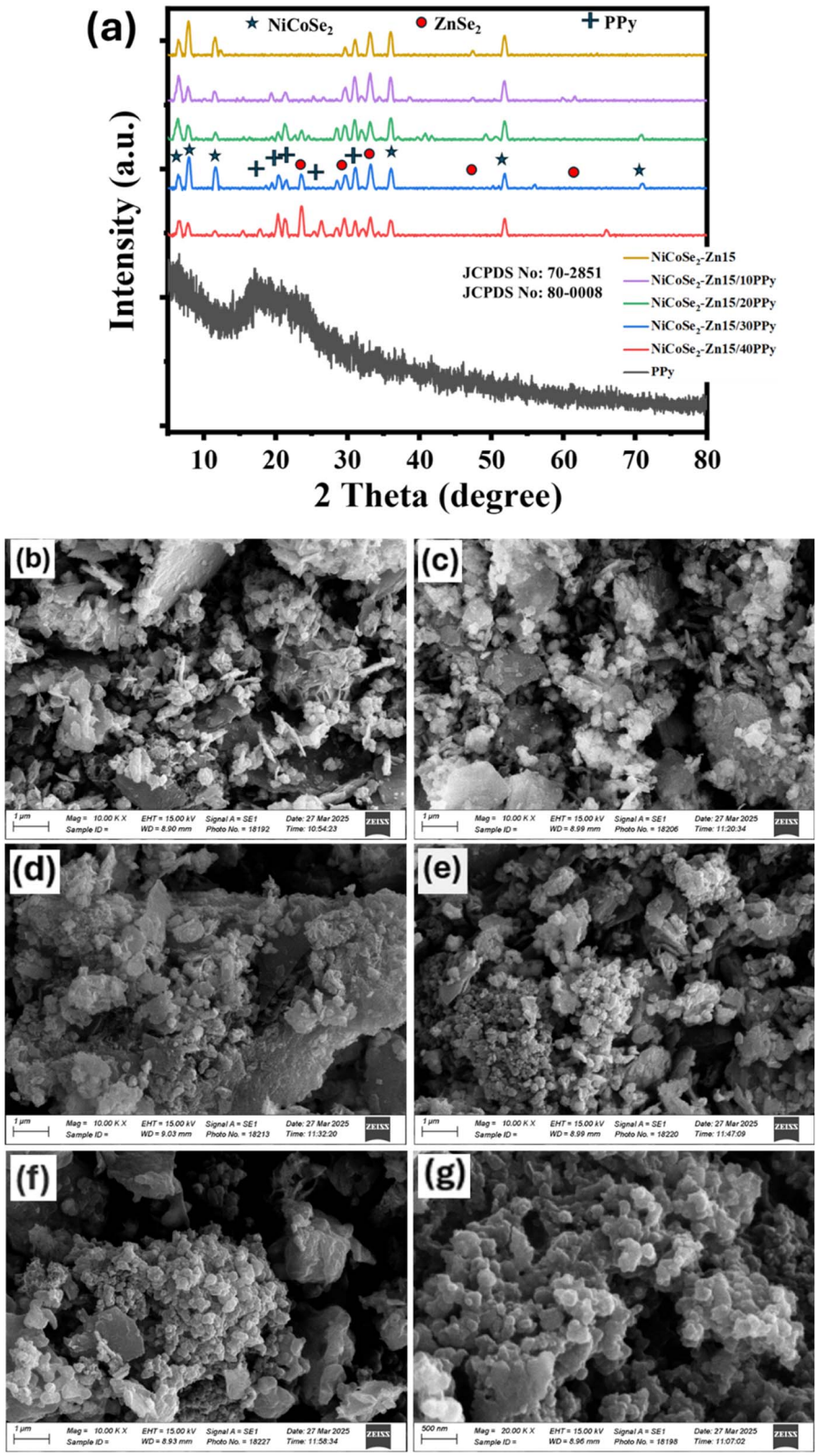

Fig. 2 (a) XRD pattern and (b–g) SEM image presenting surface morphology of synthesized selenide samples (b) $NiCoSe_2$–Zn15, (c) $NiCoSe_2$–Zn15/10PPy, (d) $NiCoSe_2$–Zn15/20PPy, (e) $NiCoSe_2$–Zn15/30PPy, (f) $NiCoSe_2$–Zn15/40PPy, and (g) PPy, respectively.

potential scan rates ranging 2 to 60 mV s^{-1}. Fig. 4(a–f) portrays the CV curves corresponding to all synthesized selenide samples. The cyclic voltammetry profiles of all samples clearly reveal the presence of two distinct current peaks (oxidation and reduction) at specific voltages in both the forward and reverse scans. The appearance of these peaks is attributed to the

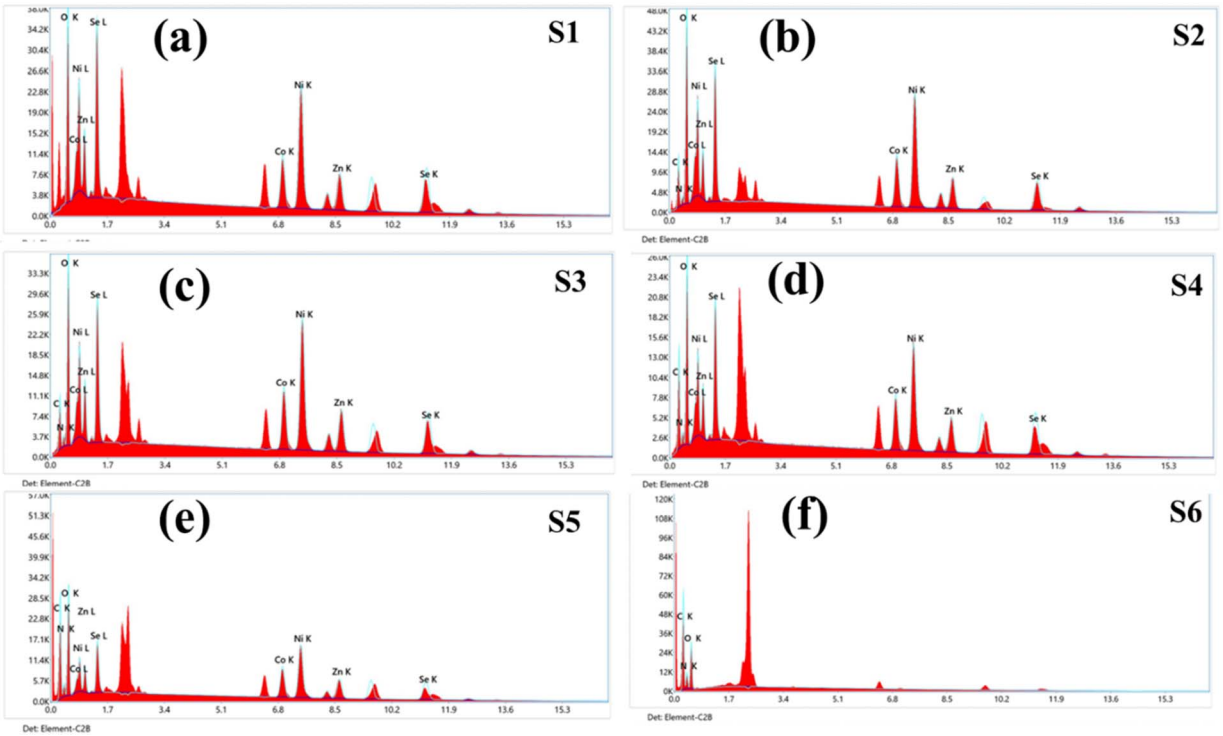

Fig. 3 EDX analysis results for the synthesized $NiCoSe_2$–Zn15/PPY composites selenide samples: (a) S1 [$NiCoSe_2$–Zn15], (b) S2 [$NiCoSe_2$–Zn15/10PPy], (c) S3 [$NiCoSe_2$–Zn15/20PPy], (d) S4 [$NiCoSe_2$–Zn15/30PPy], (e) S5 [$NiCoSe_2$–Zn15/40PPy], and (f) S6 [PPy].

faradaic redox oxidation and reduction reactions at the interface of electrode. The nature of the curves indicates the influence of an EDLC component, yet the overall electrochemical behavior of selenide electrodes suggests a redox-dominant pseudocapacitive nature. When the potential scan rate is increased, the curves maintain their symmetry while exhibiting broad peak, indicating that samples $NiCoSe_2$–Zn15, $NiCoSe_2$–Zn15/10PPy, $NiCoSe_2$–Zn15/20PPy, $NiCoSe_2$–Zn15/30PPy, $NiCoSe_2$–Zn15/40PPy, and PPy possess superior rate capability; however, with the increase of potential sweep rate the internal resistance of the fabricated electrode also increases. The shift of redox peaks toward higher voltages with increasing

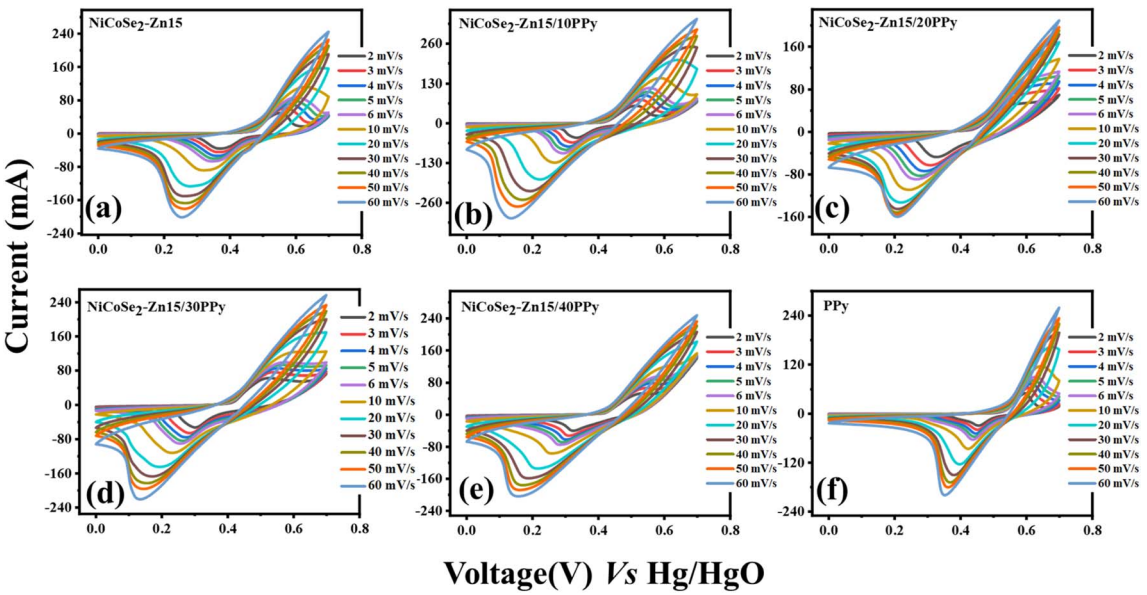

Fig. 4 CV curves of (a) $NiCoSe_2$–Zn15, (b) $NiCoSe_2$–Zn15/10PPy, (c) $NiCoSe_2$–Zn15/20PPy, (d) $NiCoSe_2$–Zn15/30PPy, (e) $NiCoSe_2$–Zn15/40PPy, and (f) PPy at different scan rates.

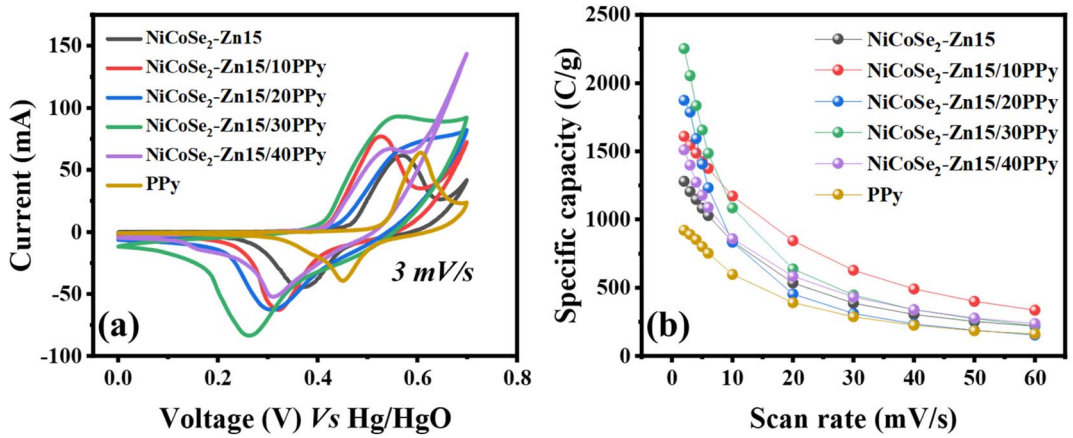

Fig. 5 (a) Comparison CV curve of all samples at 3 mV s^{-1} (b) Q_s calculated through CV curves.

potential scan rates indicates that the samples have a redox-dominant pseudocapacitive nature, a characteristic typically observed in battery-grade electrodes.

The Q_s of the electrode material can be estimated by analyzing the area enclosed by the cyclic curve. Fig. 5(a) provides a comparative representation of the voltammograms for all analyzed samples. It is evident that sample $NiCoSe_2$–Zn15/30PPy exhibits the greater area under the cyclic curve, indicating a higher retention of specific capacity (Q_s). The Q_s was derived from the CV profiles by applying following equation:[8,28]

$$Q_s = \frac{1}{mv} \times \int I \times V \mathrm{d}V \quad (2)$$

In this equation, the expression $\int I \times V\mathrm{d}V$ signifies the area covered by the CV curve, obtained by integrating the product of current (I) and voltage (V) with respect to dV. The mass of the electrode's active material is defined by m, and the scan rate is described by v. As portrays in Fig. 5(b), our results demonstrated that sample $NiCoSe_2$–Zn15/30PPy exhibits the highest specific capacity (Q_s) of 2252.6 C g^{-1} at a potential scan rate of 2 mV s^{-1}, outperforming $NiCoSe_2$–Zn15, $NiCoSe_2$–Zn15/10PPy, $NiCoSe_2$–Zn15/20PPy, $NiCoSe_2$–Zn15/40PPy, and PPy, which exhibit Q_s values of 1279.6, 1609.9, 1874.8, 1510.9, and 922.4 C g^{-1}, respectively. Various methods were employed for the theoretical analysis of the $NiCoSe_2$–Zn15/30PPy electrode material. The power law outlined below can be used to measure the b-values of hybrid devices:[8]

$$I_p = av^b \quad (3)$$

$$\log(I_p) = \log a + b \log v \quad (4)$$

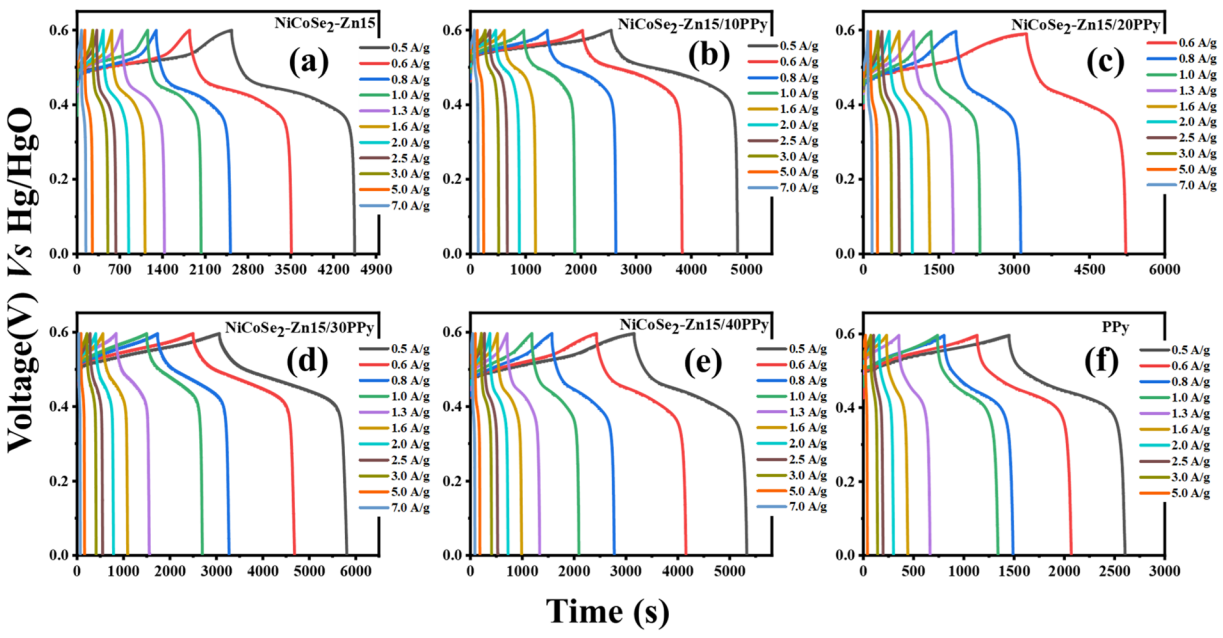

Fig. 6 Galvanostatic charge–discharge (GCD) curves recorded for (a) $NiCoSe_2$–Zn, (b) $NiCoSe_2$–Zn15/10PPy, (c) $NiCoSe_2$–Zn15/20PPy, (d) $NiCoSe_2$–Zn15/30PPy, (e) $NiCoSe_2$–Zn15/40PPy, and (f) PPy.

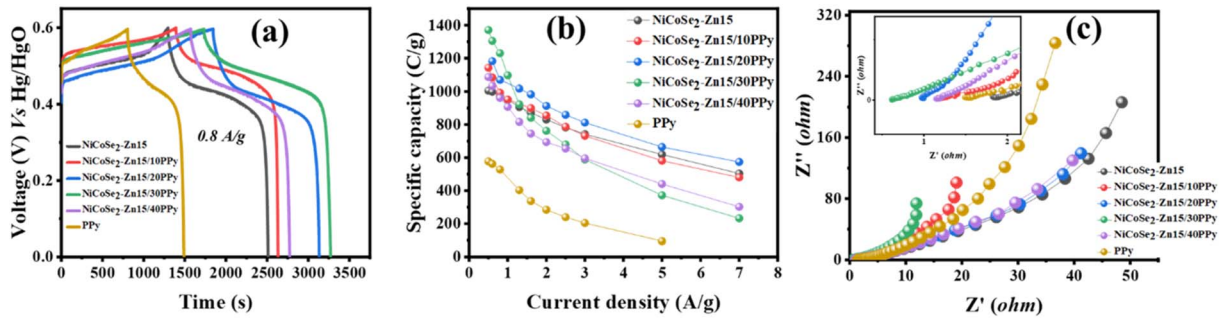

Fig. 7 (a) Comparison of GCD behavior for all samples at a current density of 0.8 A g^{-1}. (b) Current density-dependent specific capacities recorded for all samples. (c) Electrochemical impedance spectroscopy (EIS) spectra for samples all prepared electrode materials.

The electrode material exhibits the *b*-values between 0.5 and 1.0. A *b*-value of 0.5 for an electrode material suggests a battery-type charge storage behavior, while 1.0 *b*-value is indicative of a capacitive-dominant nature.[8] As shown in Fig. S1(a), the *b*-value for sample $NiCoSe_2$–Zn15/30PPy is around 0.5, confirming the redox-active nature of the $NiCoSe_2$–Zn15/30PPy material. For electrodes with diffusion-controlled charge storage, the current increases proportionally with the square root of potential scan rate.[8] As shown in Fig. S1(b), the graph with an *R* square-value of 0.98 further validates the diffusive charge storage mechanism of $NiCoSe_2$–Zn15/30PPy. The current contributions arising from diffusion-controlled and capacitive processes during electrode charging and discharging can be determined using Dunn's model, as expressed below:[44]

$$i(V) = i_{cap} + i_{dif} \quad (5)$$

$$i(V) = k_1 v + k_2 v^{\frac{1}{2}} \quad (6)$$

In this equation, '*i*' denotes the current, whereas 'k_1' and 'k_2' are arbitrary constant. As shown in Fig. S1(c), the diffusive and capacitive current at 3 mV s^{-1} are displayed, confirming the diffusion-dominant behavior of the selenide sample $NiCoSe_2$–Zn15/30PPy. The sample containing 30% PPy demonstrated the most prominent redox peaks and highest integrated area under the CV curve, signifying superior electrochemical activity. The enhanced performance can be ascribed to the synergistic effect of well-dispersed PPy within the $NiCoSe_2$–Zn15 matrix, facilitating rapid electron transport and ion diffusion. Thus, the outcomes highlight $NiCoSe_2$–Zn15/30PPy as a promising electrode material for asymmetric supercapacitors.

4.2.2. Galvanostatic charge–discharge (GCD). The charge storage capacity of the electrode material was examined using GCD measurements. The GCD analysis of all synthesized samples was conducted within a 0–0.6 V potential range at current densities of 0.5 A g^{-1} to 7.0 A g^{-1}, which was determined according to the reaction peak positions in the CV profile. As demonstrated in Fig. 6(a–f), the GCD outcomes for the selenide samples align efficiently with the CV results. A distinct plateau-like feature with a prominent hump in the charge–discharge curves of the GCD profiles suggests the occurrence of faradaic redox reactions. The specific capacities (Q_s) and specific capacitance (C_s) through GCD of these selenide samples, which were calculated based on eqn (7) and (8):[44]

$$Q_s = \Delta t \times I/m \quad (7)$$

$$C_s = \Delta t/\Delta V \times I/m \quad (8)$$

In this equation, 'I/m' corresponds to the current density, while 'Δt' and 'ΔV' signifies the total discharge time and PW of the selenide sample. Moreover, the comparison GCD profile of all the synthesized samples at 0.8 A g^{-1} is depicted in Fig. 7(a). At

Table 1 The electrochemical performance of $NiCoSe_2$–Zn15/30PPy in comparison with previously reported literature

S. no.	Electrode materials	Preparation method	Electrolyte	Potential window (V)	Specific capacity (C g^{-1})	Ref.
1	MG-CoNiSe	Electrostatic self-assemble selenization processes	6 M KOH	0 to 0.45	702.7 C g^{-1} at 1 A g^{-1}	49
2	NiSe/MnSe@CoS	Electrodeposition	2.0 M KOH	0 to 0.45	884.0 C g^{-1} at 1 A g^{-1}	50
3	$CoSe_2$/$NiSe_2$ film	Electrodeposition	3 M KCl	0 to 0.4V	646C g^{-1} at 1 A g^{-1}	51
4	$Ni_{0.5}Co_{0.5}Se_2$	Hydrothermal	1 M KOH	0 to 0.6	805.6 C g^{-1} at 1.8 A g^{-1}	52
5	$NiSe_2$–Fe_3Se_4@NiCoB	Hydrothermal	2 M KOH	0 to 0.45	887.0 C g^{-1} at 1 A g^{-1}	53
6	ZnO@CoS	Electrodeposition	3 M KOH	0 to 0.55	898.9 C g^{-1} at 3 mA cm^{-2}	54
7	$MnSe_2$@$NiCo_2Se_4$	Hydrothermal	6 M KOH	0 to 0.45	1078 C g^{-1} at 1 A g^{-1}	55
8	$CuCo_2O_4$ BMs	Hydrothermal	2 M KOH	0 to 0.4	303.22 C g^{-1} at 1 A g^{-1}	56
9	$CuCo_2O_4$ nanosheets	Hydrothermal	3 M KOH	0 to 0.45	246.0 C g^{-1} at 0.5A g^{-1}	57
10	**$NiCoSe_2$–Zn15/30PPy**	**Hydrothermal**	**1 M KOH**	**0 to 0.6**	**1370.5 C g^{-1} at 0.5 A g^{-1}**	**Present work**

a lowest current density, the specific capacities (specific capacitance) of samples $NiCoSe_2$–Zn15, $NiCoSe_2$–Zn15/10PPy, $NiCoSe_2$–Zn15/20PPy, $NiCoSe_2$–Zn15/30PPy, $NiCoSe_2$–Zn15/40PPy, and PPy were determined to be 1005.6 (1436.6), 1142.0 (1631.4), 1182.2 (1688.9), 1370.5 (1957.9), 1085.7 (1551.0), and 577.4 C g^{-1} (824.9), respectively, as depicted in Fig. 7(b) and S2. The GCD analysis also highlights the superior electrochemical performance of sample $NiCoSe_2$–Zn15/30PPy. Therefore, $NiCoSe_2$–Zn15/30PPy exhibits a significant capacity loss when the current densities are increased from 2 A g^{-1} to 7 A g^{-1}. This decline can be attributed to the increase in equivalent series resistance (ESR) at higher current densities, as well as the limited permeability of the electrode material to intercalate with the electrolytic ions, leading to sluggish ion kinetics and a sudden drop in capacity.[44,47,48] Consistent with the CV results, the 30% PPy composite exhibited the longest discharge time and highest specific capacity, confirming its superior charge storage capability. This superior behavior is linked to the synergistic effect of the conductive PPy network and porous 15% Zn doped $NiCoSe_2$ matrix, which together enhance electron mobility and electrolyte accessibility.

4.2.3. Electrochemical impedance spectroscopy (EIS). The conductive properties of the selenide samples were scrutinized through electrochemical impedance spectroscopy (EIS) within a frequency range of 0.1–100 000 Hz. Fig. 7(c) displays the EIS spectra corresponding to all mixed metal selenide-based samples (S1 to S6), with inset represents the high-frequency region of Nyquist plot. The equivalent series resistance (ESR) of each sample was determined, which represents the combined resistance from diffusion of ions through the electrolyte (KOH), the electrode material's electrical conductivity, and interfacial resistance between the electrode and electrolyte. The selenide samples demonstrate an almost insignificant equivalent series resistance (ESR). The semicircle observed in the high-frequency portion of the EIS spectrum represents the charge transfer resistance (R_{ct}), or the resistance encountered during charge transfer at the electrode. The $NiCoSe_2$–Zn15/30PPy sample exhibit negligible R_{ct} in the high-frequency portion, indicating their superior conductivity. The presence of an inclined line in the lower frequency domain corresponds to Warburg impedance (W_d) which illustrates the ion (OH^-) diffusion resistance in the selenide-based electrode material, while slope of the line also provides information about nature of the electrode material. The ESR of an electrode material is determined by the x-intercept of the EIS profile at high frequencies. For samples $NiCoSe_2$–Zn15, $NiCoSe_2$–Zn15/10PPy, $NiCoSe_2$–Zn15/20PPy, $NiCoSe_2$–Zn15/30PPy, $NiCoSe_2$–Zn15/40PPy, and PPy, the ESR values were calculated as 1.83 Ω, 1.17 Ω, 0.99 Ω, 0.62 Ω, 1.19 Ω, and 1.49 Ω, respectively. The 30% PPy composite exhibited the lowest equivalent series resistance in the EIS analysis,

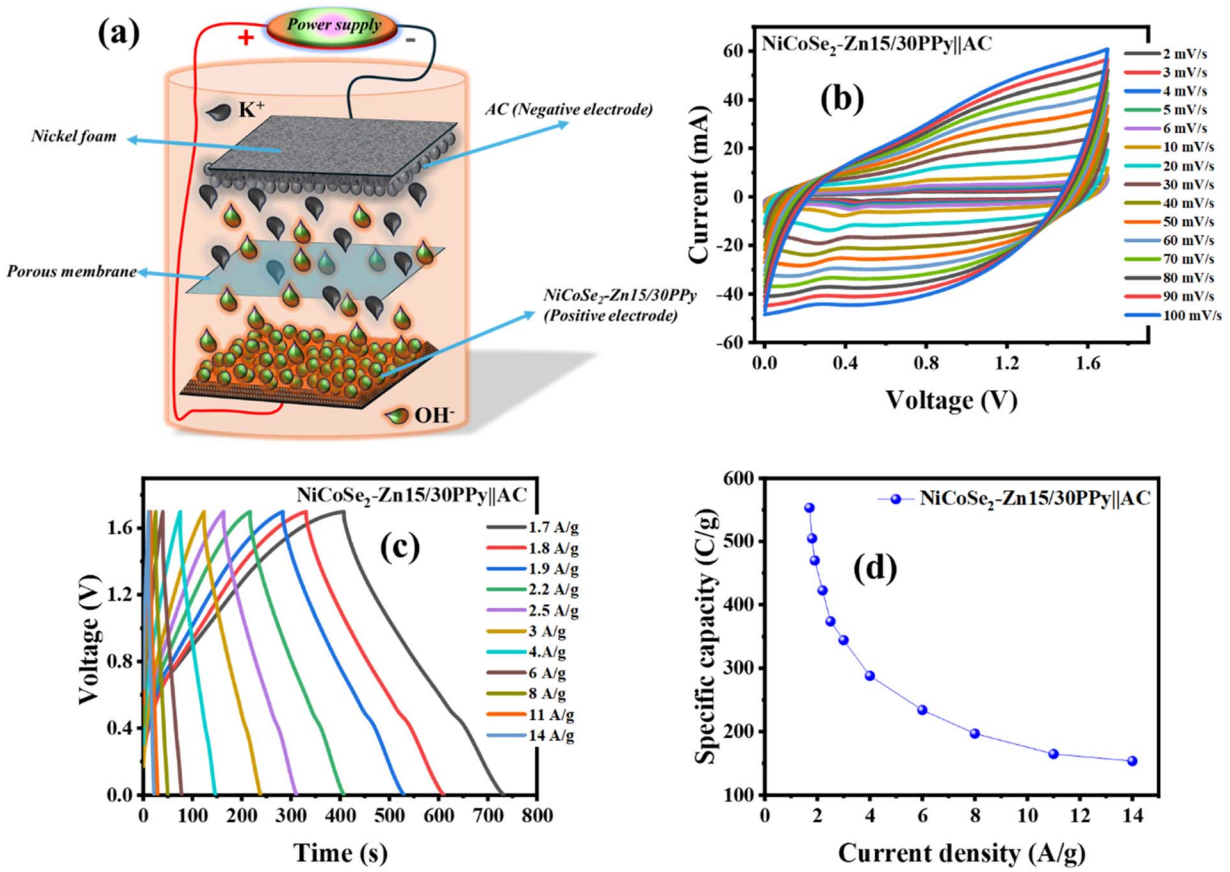

Fig. 8 (a) Illustrative depiction of structurally engineered hybrid (NiCoSe2–Zn15/30PPY||AC) supercapacitors. (b) CV represents the behavior of the $NiCoSe_2$–Zn15/30PPY||AC. (c) GCD profile of the hybrid device. (d) Q_s calculated through GCD of the real device.

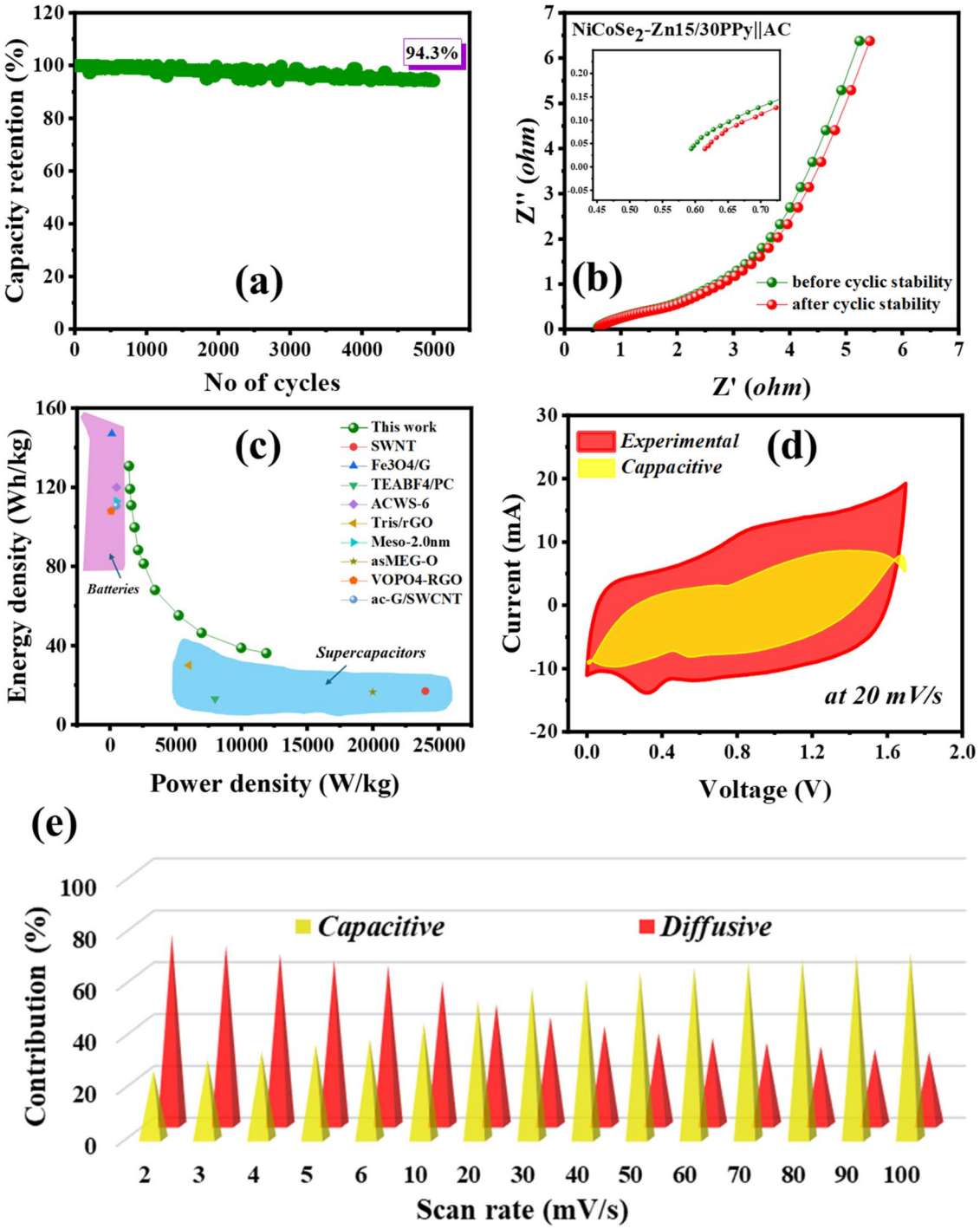

Fig. 9 (a) Calculated cyclic stability of fabricated $NiCoSe_2$–Zn15/30PPY||AC device during 5000 cycles. (b) Device EIS analysis with inset of high frequency region. (c) Ragone plot of the $NiCoSe_2$–Zn15/30PPY||AC device with reported literature. (d) Capacitive contributions of the hybrid device at scan rates of 20 mV s^{-1}. (e) Sweep rate-dependent analysis of capacitive and diffusion-controlled contributions.

confirming its superior electrical conductivity and enhanced interfacial charge transport. Table 1 presents a comparison of the electrochemical performance of $NiCoSe_2$–Zn15/30PPy in a three-electrode configuration with already reported literature. The outstanding electrochemical response exhibited by sample $NiCoSe_2$–Zn15/30PPy suggests its potential use as a battery-grade electrode in hybrid (Asymmetric) supercapacitor systems.

4.3. Hybrid (asymmetric) supercapacitors

A hybrid supercapacitor was fabricated to investigate the feasibility of selenide sample ($NiCoSe_2$–Zn15/30PPy) in practical applications, employing sample $NiCoSe_2$–Zn15/30PPy and AC as a positive electrode and negative electrode, respectively (Fig. 8(a)). Electrochemical characterization of the assembled $NiCoSe_2$–Zn15/30PPy||AC hybrid device was conducted through

CV. In three-electrode setup, the potential window (PW) for AC was established as 0 to −1 V, whereas $NiCoSe_2$–Zn15/30PPy exhibited an operational range of 0 to 0.7 V. Fig. S3(a) portrays the CV curve of $NiCoSe_2$–Zn15/30PPy (from 0 to 0.7 V) and AC (from 0 to −1 V) at 3 mV s^{-1}. The optimal PW of 0 to 1.7 V was carefully selected for the CV analysis to ensure precise measurements. The results obtained across potential sweep rates from 2 to 100 mV s^{-1} were visually represented in Fig. 8(b). The CV profiles of the hybrid device exhibit a distinctive shape, confirming its hybrid features. The CV curves maintain their symmetrical nature even at elevated scan rates, exhibiting the outstanding stability and high-rate capability of the hybrid device. Fig. S3(b) represents the cyclic curves of the hybrid supercapacitors at different PWs of 0.6, 0.8, 1.0, 1.2, 1.4, 1.5, 1.6, and 1.7 V. In addition, GCD tests were performed at different current density (1.7–14 A g^{-1}) within a PW of 0–1.7 V. The results from the GCD analysis were in very good agreement with the CV measurements, as depicted in Fig. 8(c). The presence of nonlinear features in the GCD profile provides clear confirmation of the hybrid characteristics of the device. As shown in Fig. S3(c), GCD performed at different PW to optimize the operational potential window for a hybrid device. As illustrated in Fig. 8(d), the $NiCoSe_2$–Zn15/30PPy||AC device exhibited an optimal specific capacity (Q_s) of 553.5 C g^{-1} at 1.7 A g^{-1}.

To evaluate the cyclic stability of the fabricated hybrid device, it was subjected to 5000 consecutive GCD cycles at 14 A g^{-1}. The hybrid supercapacitor revealed excellent cycling stability, preserving 94.3% of its initial charge capacity (Fig. 9(a)). The conductive nature of the $NiCoSe_2$–Zn15/30PPy||AC device was investigated through EIS measurements before and after the stability testing (Fig. 9(b)). The electrochemical impedance response of the electrode was examined through EIS in a frequency range of 0.1–100 000 Hz. The ESR value of the hybrid device increased from 0.59 Ω to 0.61 Ω after the cycling stability. The slight rise in electrochemical resistance is ascribed to continuous faradaic reactions occurring over 5000 charge–discharge cycles.[28,58] Furthermore, the obtained R_{ct} value was nearly negligible (inset of Fig. 9(b)). Specific energy density (E_s) and specific power density (P_s) are two primary metrics governing energy storage performance. These parameters for the fabricated device were evaluated based on eqn (9) and (10):[44,59]

$$E_s = Q_s \times \Delta V/7.2 \quad (9)$$

$$P_s = E_s \times 3600/\Delta t \quad (10)$$

The $NiCoSe_2$–Zn15/30PPy||AC hybrid device demonstrated an optimal energy storage performance, attaining a maximum specific E_s of 130.7 Wh kg^{-1} at P_s of 1449.8 W kg^{-1} and a maximum specific P_s of 11 900 W kg^{-1} at 36.2 Wh kg^{-1}, as depicted in Fig. 9(c). These findings demonstrate superior performance when compared to previously reported results in the literature, such as SWNT, Fe_3O_4/G, TEABF4/PC, ACWS-6, Tris/rGO, Meso-2.0 nm, asMEG-O, $VOPO_4$-RGO, and ac-G/SWCNT.[60–68] Fig. S3(d) presents the *b*-value fitting (power's law) across various voltages from 1 to 1.6 V. The hybrid device reveals *b*-values ranging between 0.73 and 0.83. An intermediate range of *b*-values, from 0.5 to 0.8 is observed in the hybrid device (inset of Fig. S3(d)), commonly referred to as an asymmetric configuration.[8,69]

To obtain theoretical interpretations of the fabricated $NiCoSe_2$–Zn15/30PPy||AC device, Dunn's model was implemented using eqn (6). Fig. 9(d) displays the capacitive contribution of 53.4%, whereas diffusive current contributions of 46.6% at scan rate of 20 mV s^{-1}. At scan rates of 3, 60, and 100 mV s^{-1}, the capacitive (diffusion-controlled) contributions are 30.7% (69.3%), 66.5% (33.5%), and 71.9% (28.1%), respectively (Fig. S4(a–c)). Furthermore, the overall percentage contribution of current at distinct scan rates are shown in Fig. 9(e). The findings provide strong evidence for the enhanced hybrid features of the fabricated $NiCoSe_2$–Zn15/30PPy||AC device.

5. Conclusions

In conclusion, the hydrothermal synthesis technique was employed for the preparation of $NiCoSe_2$–15Zn, while PPy was incorporated through a simple physical mixing approach. Structural and morphological analyses have confirmed the effective synthesis of the prepared materials. The electrochemical performance of all electrodes was examined in three-electrode configuration, where $NiCoSe_2$–Zn15/30PPY demonstrated the highest specific capacities than other composite, achieving 2252.6 C g^{-1} at 2 mV s^{-1} and 1370.5 C g^{-1} at 0.5 A g^{-1}. The optimized electrodes were utilized into an asymmetric supercapacitor (ASC) device, specifically $NiCoSe_2$–Zn15/30PPY||AC demonstrating outstanding energy and power densities. The device reached a remarkable E_s of 130.7 Wh kg^{-1} at 0.5 A g^{-1} while maintaining a P_s of 1449.8 W kg^{-1}, and even at an elevated current density of 14 A g^{-1}, it retained 36.2 Wh kg^{-1} and 11 900 W kg^{-1}. The results emphasize the superior specific capacity of the device. Furthermore, it showcased excellent cyclic stability, retaining 94.3% of its original capacity after 5000 cycles. To confirm the battery-grade performance of the supercapacitor, the power law analysis was conducted, revealing that the *b*-values of the electrodes fall within the range of 0.5 to 1. These findings establish binary $NiCoSe_2$–Zn15/30PPY as a promising candidate for various applications, such as renewable energy storage and electric vehicles.

Conflicts of interest

There are no conflicts to declare.

Data availability

There is not used any external data in this study. And all the relevant experimental data has already been included and thoroughly discussed in the main manuscript.

Supplementary information is available, which includes additional electrochemical results. See DOI: **https://doi.org/10.1039/d5ra04328j**.

Acknowledgements

This work was supported by the Ghulam Ishaq Khan Institute of Engineering Sciences and Technology, Pakistan (https://www.giki.edu.pk) *via* its graduate assistantship scheme (GA-4) awarded to Anique Ahmed with Reg. # ES2203.

References

1 M. Muratori, M. Alexander, D. Arent, M. Bazilian, P. Cazzola, E. M. Dede, J. Farrell, C. Gearhart, D. Greene and A. Jenn, *Prog. Energy*, 2021, **3**, 022002.
2 G. G. Njema, R. B. O. Ouma and J. K. Kibet, *J. Renewable Energy*, 2024, **2024**, 2329261.
3 M. A. Dar, S. Majid, M. Satgunam, C. Siva, S. Ansari, P. Arusalan and S. R. Ahamed, *Int. J. Hydrogen Energy*, 2024, **70**, 10–28.
4 L. Liu, X. Zhang, Y. Liu and X. Gong, *ACS Appl. Electron. Mater.*, 2025, **7**, 2233–2270.
5 H. T. A. Awan, M. A. A. M. Abdah, M. Mehar, R. Walvekar, V. Chaudhary, M. Khalid and A. Khosla, *J. Energy Storage*, 2024, **95**, 112449.
6 R. T. Yadlapalli, R. R. Alla, R. Kandipati and A. Kotapati, *J. Energy Storage*, 2022, **49**, 104194.
7 A. G. Olabi, Q. Abbas, A. Al Makky and M. A. Abdelkareem, *Energy*, 2022, **248**, 123617.
8 A. Ahmed, M. R. Abdul Karim and M. Usman, *Energy Technol.*, 2025, **13**, 2401761.
9 S. R. Khaladkar, O. Maurya, G. Gund, B. Sinha, D. Dubal, R. Deshmukh and A. Kalekar, *ACS Appl. Mater. Interfaces*, 2024, **16**, 11408–11420.
10 C. V. M. Gopi, D. K. Kulurumotlakatla, K. Raghavendra, M. Suneetha and R. Ramesh, *RSC Adv.*, 2024, **14**, 40087–40097.
11 T. Song, Y. Zhao, C. Chen, X. Gui, X. Wu and X. Wang, *J. Energy Storage*, 2024, **98**, 113148.
12 K. Kavya, K. Kalawat, P. Kour, S. Kour and A. Sharma, *Mater. Res. Bull.*, 2025, **184**, 113270.
13 R. A. Mir, J. Xu, L. Tao, E. J. Hansen, A. Khosrozadeh, M. B. Miller and J. Liu, *Nano Energy*, 2025, **133**, 110446.
14 J. Duay, E. Gillette, R. Liu and S. B. Lee, *Phys. Chem. Chem. Phys.*, 2012, **14**, 3329–3337.
15 Z. Ayaganov, V. Pavlenko, S. F. B. Haque, A. Tanybayeva, J. Ferraris, A. Zakhidov, Z. Mansurov, Z. Bakenov and A. Ng, *J. Energy Storage*, 2024, **78**, 110035.
16 M. Girirajan, A. K. Bojarajan, I. N. Pulidindi, K. N. Hui and S. Sangaraju, *Coord. Chem. Rev.*, 2024, **518**, 216080.
17 N. Muzaffar, A. M. Afzal, M. W. Iqbal, A. Yasmeen, M. D. Albaqami, S. M. Wabaidur, S. Mumtaz and S. A. Munnaf, *J. Mater. Sci.: Mater. Electron.*, 2024, **35**, 1–16.
18 Z. A. Sheikh, D. Vikraman, H. Kim, I. Hussain, G. Nazir, S. F. Shaikh, H.-S. Kim, J. Jung, S. Hussain and D.-K. Kim, *Renewable Energy*, 2025, 122418.
19 A. K. Singh, in *2D Transition-Metal Dichalcogenides (TMDs): Fundamentals and Application*, Springer, 2025, pp. 1–65.
20 A. K. Singh, *2D Transition-Metal Dichalcogenides (TMDs): Fundamentals and Application*, Springer Nature, 2025.
21 I. Hussain, S. Sahoo, C. Lamiel, T. T. Nguyen, M. Ahmed, C. Xi, S. Iqbal, A. Ali, N. Abbas and M. S. Javed, *Energy Storage Mater.*, 2022, **47**, 13–43.
22 Y. Zhang, J. Guo, J. Ren, Z. Chen, M. Zhang and Z. Li, *J. Alloys Compd.*, 2023, **951**, 169820.
23 X. Wang, X. Zhang, Y. Zhao, D. Luo, L. Shui, Y. Li, G. Ma, Y. Zhu, Y. Zhang and G. Zhou, *Angew. Chem.*, 2023, **135**, e202306901.
24 X. Yun, T. Lu, R. Zhou, Z. Lu, J. Li and Y. Zhu, *Chem. Eng. J.*, 2021, **426**, 131328.
25 S. Shanmugan, *Novel Energy Storage and Conversion Technologies for Two-Dimensional MXenes and MBenes*, 2025, vol. 77.
26 Q. Fu, J. Han, X. Wang, P. Xu, T. Yao, J. Zhong, W. Zhong, S. Liu, T. Gao and Z. Zhang, *Adv. Mater.*, 2021, **33**, 1907818.
27 P. Prabhu, V. Jose and J.-M. Lee, *Matter*, 2020, **2**, 526–553.
28 A. Ahmed, M. R. A. Karim and M. Usman, *Electrochim. Acta*, 2025, 145764.
29 M. Ahmad, I. Hussain, T. Nawaz, Y. Li, X. Chen, S. Ali, M. Imran, X. Ma and K. Zhang, *J. Power Sources*, 2022, **534**, 231414.
30 Z. Lu, Z. Hu, L. Xiao, Y. Xie, N. Li, L. Xi, W. Chen, J. Xiao and Y. Zhu, *Chem. Eng. J.*, 2022, **450**, 138347.
31 S. Ghosh, P. Samanta, N. C. Murmu and T. Kuila, *J. Alloys Compd.*, 2020, **835**, 155432.
32 Y. Gong, Y. Li, Y. Li, M. Liu, Y. Bai and C. Wu, *Small*, 2023, **19**, 2206194.
33 X. Chen, Q. Liu, T. Bai, W. Wang, F. He and M. Ye, *Chem. Eng. J.*, 2021, **409**, 127237.
34 X. Jia, C. Liu, Z. G. Neale, J. Yang and G. Cao, *Chem. Rev.*, 2020, **120**, 7795–7866.
35 J. Hao, X. Li, X. Zeng, D. Li, J. Mao and Z. Guo, *Energy Environ. Sci.*, 2020, **13**, 3917–3949.
36 L. E. Blanc, D. Kundu and L. F. Nazar, *Joule*, 2020, **4**, 771–799.
37 S. K. Kandasamy and K. Kandasamy, *J. Inorg. Organomet. Polym. Mater.*, 2018, **28**, 559–584.
38 K. Namsheer and C. S. Rout, *RSC Adv.*, 2021, **11**, 5659–5697.
39 G. Tang, J. Liang and W. Wu, *Adv. Funct. Mater.*, 2024, **34**, 2310399.
40 M. Xu, S. Cui, X. Fu, C. Zhang, G. Li and L. Han, *ACS Appl. Nano Mater.*, 2025, **8**, 6454–6464.
41 C. Koning, M. Van Duin, C. Pagnoulle and R. Jerome, *Prog. Polym. Sci.*, 1998, **23**, 707–757.
42 A. Pud, N. Ogurtsov, A. Korzhenko and G. Shapoval, *Prog. Polym. Sci.*, 2003, **28**, 1701–1753.
43 B. Kirubasankar, V. Murugadoss, J. Lin, T. Ding, M. Dong, H. Liu, J. Zhang, T. Li, N. Wang and Z. Guo, *Nanoscale*, 2018, **10**, 20414–20425.
44 A. Ahmed, M. R. Abdul Karim and M. Usman, *Electrochim. Acta*, 2025, **531**, 146351.
45 Y. Wang, J. Yang, L. Wang, K. Du, Q. Yin and Q. Yin, *ACS Appl. Mater. Interfaces*, 2017, **9**, 20124–20131.
46 A. U. Rehman, A. M. Afzal, M. W. Iqbal, M. Imran and M. Ali, *Polym. Sci., Ser. A*, 2023, **65**, 447–471.
47 Y. Shao, M. F. El-Kady, J. Sun, Y. Li, Q. Zhang, M. Zhu, H. Wang, B. Dunn and R. B. Kaner, *Chem. Rev.*, 2018, **118**, 9233–9280.

48 E. Mourad, L. Coustan, P. Lannelongue, D. Zigah, A. Mehdi, A. Vioux, S. A. Freunberger, F. Favier and O. Fontaine, *Nat. Mater.*, 2017, **16**, 446–453.
49 J. Chen, T. Song, M. Sun, S. Qi, C. Chen, Y. Zhao and X. Wu, *J. Alloys Compd.*, 2024, **1009**, 176786.
50 L. Wan, G. Ye, Y. Zhang, J. Chen, C. Du and M. Xie, *Appl. Surf. Sci.*, 2024, **670**, 160638.
51 Y.-H. Lee, J. S. Kang, I.-R. Jo, Y.-E. Sung and K.-S. Ahn, *J. Electroanal. Chem.*, 2021, **895**, 115479.
52 A. Ahmed, M. R. Abdul Karim and M. Usman, *Electrochim. Acta*, 2025, **517**, 145764.
53 Z. Tian, K. Zhou, M. Xie, Y. Zhang, J. Chen, C. Du and L. Wan, *Chem. Eng. J.*, 2022, **447**, 137495.
54 S. Ding, X. Li, X. Jiang, Q. Hu, Y. Yan, Q. Zheng and D. Lin, *Electrochim. Acta*, 2020, **354**, 136711.
55 X. Sun, K. Zhao, H. Fu, H. Guo, J. Shen, F. Jin, L. Wang, Z. Wang, L. Cui, F. Quan and J. Liu, *J. Energy Storage*, 2023, **63**, 107041.
56 J. Sun, X. Du, R. Wu, Y. Zhang, C. Xu and H. Chen, *ACS Appl. Energy Mater.*, 2020, **3**, 8026–8037.
57 R. S. Babu, R. Vinodh, A. De Barros, L. Samyn, K. Prasanna, M. Maier, C. Alves and H.-J. Kim, *Chem. Eng. J.*, 2019, **366**, 390–403.
58 Y. Wang, Y. Song and Y. Xia, *Chem. Soc. Rev.*, 2016, **45**, 5925–5950.
59 A. Ahmed, M. R. A. Karim and M. Usman, *Electrochim. Acta*, 2025, 146351.
60 A. Izadi-Najafabadi, S. Yasuda, K. Kobashi, T. Yamada, D. N. Futaba, H. Hatori, M. Yumura, S. Iijima and K. Hata, *Adv. Mater.*, 2010, **22**, E235–E241.
61 F. Zhang, T. Zhang, X. Yang, L. Zhang, K. Leng, Y. Huang and Y. Chen, *Energy Environ. Sci.*, 2013, **6**, 1623–1632.
62 Y.-W. Chi, C.-C. Hu, H.-H. Shen and K.-P. Huang, *Nano Lett.*, 2016, **16**, 5719–5727.
63 T. Shang, Y. Xu, P. Li, J. Han, Z. Wu, Y. Tao and Q.-H. Yang, *Nano energy*, 2020, **70**, 104531.
64 B. Song, J. Zhao, M. Wang, J. Mullavey, Y. Zhu, Z. Geng, D. Chen, Y. Ding, K.-s. Moon and M. Liu, *Nano Energy*, 2017, **31**, 183–193.
65 X. Wang, A. Y. Mehandzhiyski, B. Arstad, K. L. Van Aken, T. S. Mathis, A. Gallegos, Z. Tian, D. Ren, E. Sheridan and B. A. Grimes, *J. Am. Chem. Soc.*, 2017, **139**, 18681–18687.
66 T. Kim, G. Jung, S. Yoo, K. S. Suh and R. S. Ruoff, *ACS Nano*, 2013, **7**, 6899–6905.
67 K. H. Lee, Y.-W. Lee, S. W. Lee, J. S. Ha, S.-S. Lee and J. G. Son, *Sci. Rep.*, 2015, **5**, 13696.
68 X. Yang, C. Cheng, Y. Wang, L. Qiu and D. Li, *Science*, 2013, **341**, 534–537.
69 R. Li and J. Liu, *Electrochim. Acta*, 2014, **120**, 52–56.